Tellus (1999), 51A, 865–879
Printed in UK. All rights reserved

TELLUS
ISSN 0280–6495

A case study of strong winds at an Arctic front

By SIGBJØRN GRØNÅS* and PAUL SKEIE, *Geophysical Institute, University of Bergen, Allégaten 70, 5007 Bergen, Norway*

(Manuscript received 28 September 1998; in final form 25 May 1999)

ABSTRACT

Shallow arctic fronts frequently form at the edge of the arctic sea–ice by differential heating and cooling between sea and ice surfaces. The cooling is due to a net radiative loss over the ice, while the heating is mainly sensible as cold air flows from the ice to the warmer sea. North of the surface fronts, there is normally a low-level jet with maximum easterly winds at the top of the boundary layer. It is shown from numerical simulations of a real case, that the low-level jet can reach hurricane force when interacting with easterly winds connected to extratropical cyclones. Strong wind is found both at an arctic front over the sea some distance from the ice edge, and at a secondary front at the ice edge. When the flow is from the ice to the sea, the sensible heating of the boundary layer is almost in balance with the cold-air advection. The convergence of the sensible heat flux amounts to a heating rate of more than 10 Kelvin per hour. The fronts are maintained by cross-frontal vertical circulations.

1. Introduction

A compilation of Norwegian ship disasters in the Arctic during this century counts 56 lost vessels (Kari Wilhelmsen, personal communication). Altogether, 342 people perished in the accidents, a high number considering the relatively low traffic in the area. In some incidents, several ships went down in the same storm. The worst case took place in March 1928 when altogether 20 vessels were lost. Wilhelmsen has suggested that the accidents were related to strong winds directly, or indirectly by severe ocean waves, icing or packing of the sea–ice. It is well known that polar lows might produce strong winds over open arctic sea areas. Similarly, strong corner jets, extending far downstream from arctic islands like Spitsbergen, have been reported (Skeie and Grønås, 1999). In this paper, it is shown that very strong winds might also be associated with shallow arctic fronts (AFs) formed at the sea–ice edge or in arctic coastal areas with open sea. The main geographical area for this study is the ocean between Norway and Spitsbergen (Fig. 1). It is shown that strong winds at AFs are associated with extratropical cyclones moving northeasterly from the

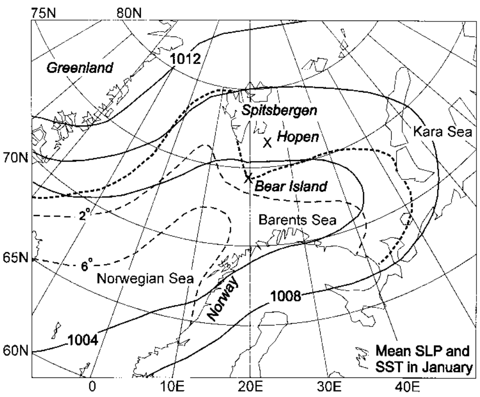

Fig. 1. Mean sea level pressure (SLP), mean sea surface temperature (SST) and mean extension of the sea–ice in the Norwegian and Barents Seas in January. From Furevik (1998).

* Corresponding author.
E-mail: sigbjorn@gfi.uib.no

Norwegian into the Barents and Kara Seas along the mean surface pressure trough shown in Fig. 1 (Serreze, 1993).

It is well-established that strong arctic inversions, with tops reaching 1000–2000 m, are present every day in winter over the interior of the sea–ice and arctic continents (Serreze, 1992). The earliest measurements of temperature and humidity profiles of the inversions were made by the Norwegian Maud Expedition (Sverdrup, 1933) and the first theoretical considerations were given by Wexler (1936) who studied the effect of radiative cooling, the main physical process. In addition, warm air advection, subsidence, cloud processes, surface melting and topography play a role in the formation of the inversions (Vowinkel and Orvig, 1970; Maykut and Church, 1973; Busch et al.; 1982; Curry, 1983). An excellent review of research on arctic inversions has recently been given by Curry et al. (1996). When the surface wind is sufficiently strong, a shallow boundary layer with neutral stratification is formed over the ice with an elevated inversion aloft. Close to the ice edge, the wind is relatively strong and elevated inversions are frequent. AFs are defined as shallow fronts at the ice edge, between cold arctic air masses below the Arctic inversion and the much warmer air masses over the sea. In this way the frontal zone is the extension of the elevated arctic inversion with very strong static stability, down to the surface. The reader should note that the expression arctic front has also been connected to the frequent wintertime extratropical cyclones in the Arctic, e.g., up the Norwegian and the Barents Sea, which have normal jets at the top of the troposphere. The deep tropospheric frontal structures have been referred to as the arctic front, a baroclinic zone in addition to the polar front (Shapiro, 1994).

General theoretical understanding of the formation and evolution of fronts is reviewed in textbooks (Holton, 1992; Bluestein, 1992; Carlson, 1991). The theory is based on the Sawyer–Eliassen equation and semi-geostrophic dynamics (Sawyer, 1956; Eliassen, 1952, 1959, 1962, 1990; Hoskins and Bretherton, 1972; Thorpe and Emanuel, 1985). In this context, under the assumption of positive potential vorticity, fronts are formed as the atmospheric response to larger scale geostrophic deformation (horizontal shear and stretching deformation) and/or gradients in diabatic heating, surface friction and orography. Differential cooling between the ice and sea is a main forcing for the arctic frontal circulation. Since large amounts of sensible heat are transferred to the atmosphere when arctic air masses propagate over the relatively warmer sea, differential sensible heating will also yield strong additional frontogenetic forcing. The significance of the frontogenetical sensible heating has recently been studied by Økland (1998).

The Bergen-school and later the Chicago-school meteorologists were aware of the AFs and observed them for instance as cold fronts over northern Europe linked to outbreaks of arctic air with associated convective activity (Godske et al., 1957; Newton and Palmén, 1969). Such outbreaks, where heating from the ocean rapidly transform the arctic air mass temperature characteristics, are referred to as arctic outbreaks (AOs). Radiosonde observations and later satellite images gave more evidence of these fronts and outbreaks. The first detailed mesoscale research aircraft measurements of AFs were made in February 1984 by the Arctic Cyclone Expedition (Shapiro et al., 1987). In 2 cases, this United States NOAA expedition made measurements from a research aircraft south of Spitsbergen. The main observations were made with dropsondes, but several other in situ and remote sensing methods were applied. Analyses of the data have been reported upon by Shapiro et al. (1989) and Shapiro and Fedor (1989).

In the present paper, a case with strong wind at an AF is studied through simulations with the Norwegian limited area weather prediction model NORLAM. A brief review of the NORLAM model and the experiment settings are found in Section 2. In the selected case, a Norwegian coast guard vessel located about 150 km south of Bear Island was surprised by hurricane force ($>32\ \mathrm{m\,s^{-1}}$) northeasterly wind in the early morning of 12 January 1993. Our simulations, discussed in Section 3, gave a realistic prediction of the strong wind. Analyses of the simulations show that the high wind was caused by interaction of an easterly low-level jet connected to an AF and easterly flow in front of a warm occlusion approaching from the south. The flow of the arctic air over the warm sea is shown to be in close balance with the intense heating from the ocean, heating which reaches rates of more than 10 Kelvin per hour ($\mathrm{K\,h^{-1}}$). At the ice edge further north, another more shallow front also possesses strong wind. Concluding remarks are contained in Section 4.

2. The numerical model

The Norwegian limited area model (NORLAM) has been used. It is described in Grønås and Hellevik (1982), Nordeng (1986) and Grønås et al. (1987). The model is hydrostatic and configured in σ-coordinates on a polar stereographic projection. The surface boundary-layer parameterisation follows Louis (1979). The Charnock relation is applied in the formulation of the ocean roughness length. The roughness length over the sea–ice is set to 0.1 m. The radiation-, cloud- and precipitation schemes are according to Nordeng (1986). A second order Shapiro filter (Haltiner and Williams, 1980) is used every hour to remove noise.

The simulations were run on two different integration domains. Both domains cover 151×121 grid points horizontally with grid lengths at 60°N of 25 and 10 km. 40 layers were distributed unevenly in the vertical with 23 layers below 700 hPa. ECMWF analyses have been used as initial conditions and to force the lateral boundaries. The sea–ice data and the sea surface temperatures, both held constant during the simulations, were provided by Det Norske meteorologiske institutt (DNMI). All experiments were initiated at 00 UTC 11 January 1993.

3. The simulation of the strong wind

At 00 UTC 12 January 1993, there was a strong northeasterly surface flow to the north of a frontal system between northern Norway and Spitsbergen. The synoptic observations of closest proximity to the naval vessel were made at Bear Island and Hopen, but none of these stations measured wind of hurricane force. The strongest wind (32.6 m s^{-1}) was measured by the ship at 00 and 03 UTC 12 January. The surface winds at Bear Island were much weaker, but the radiosounding shows winds of similar strength aloft in a well-mixed boundary layer (Fig. 4). It is the authors' belief that the surface measured winds at Bear Island are too weak to be representative of the winds over the sea and that the band of strong wind is broader than indicated by the observations. Bear Island is 15 km wide and the hills, extending to 300–500 m, are likely to influence the measurements considerably.

3.1. The development of the strong winds

The simulations with 10 km and 25 km horizontal grid distance gave qualitatively the same results. The main difference between the two simulations concerns the timing of the development, which is well predicted in the 10 km run. In the 25 km simulation the development is slower, in particular the drop in wind intensity is about 6 h too slow. However, the 25 km simulation captures more of the large scale development due to the size of the integration domain and unless otherwise stated, the following discussion relates to this simulation. Observed and simulated surface wind, pressure and temperature for the 2 runs are shown in Fig. 3 for the ship and Bear Island for synoptic times around 00 UTC 12 January. The observed and predicted wind, temperature and humidity profiles for Bear Island at 00 UTC are shown in Fig. 4.

The development of the strong winds are captured by the simulations. Furthermore, the vertical structure of the temperature field with its elevated

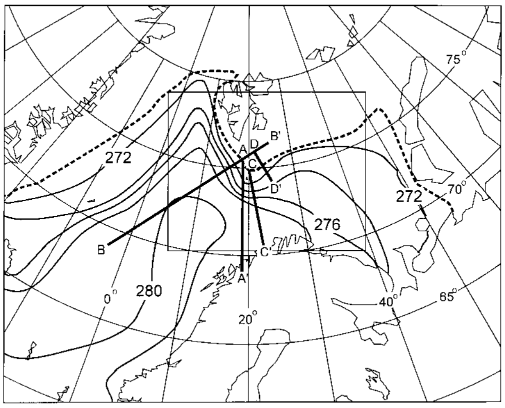

Fig. 2. The 2 integration areas, the one with 25-km grid length in the total area and the one with 10-km grid length in the inner area. Shown also are the actual SST (K) and the extent of the sea–ice used in the integrations. The data are taken from The Norwegian Meteorological Institute's operational analyses. In addition, the positions of the cross-sections used in the paper are shown.

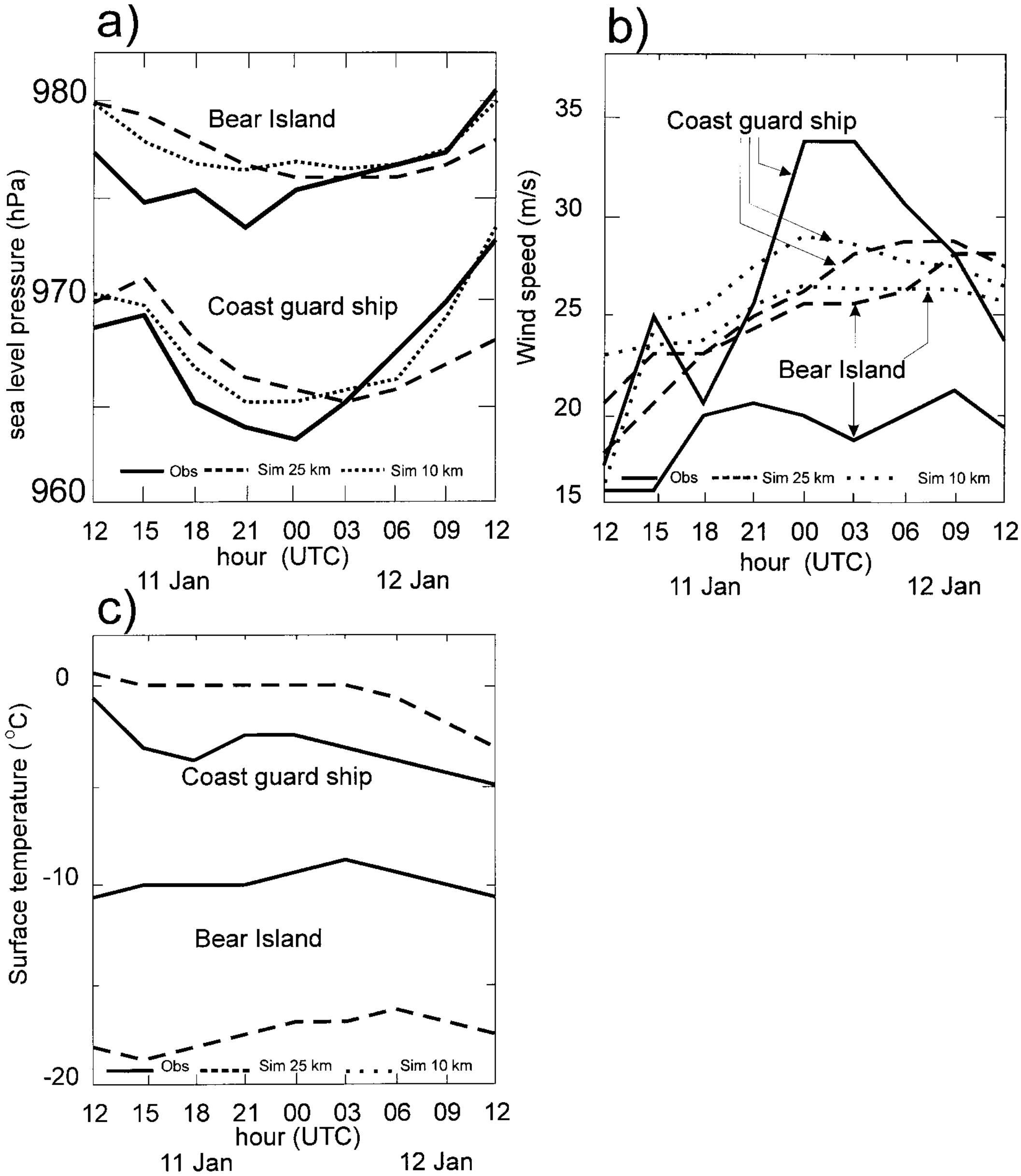

Fig. 3. Observed and simulated parameters at the surface at Bear Island and the coast guard ship (positions varying from 72 to 73°N and from 17 to 21°E) every 3 h during 24 h from 11 January 1993 12 UTC. The simulations were initialised by ECMWF analyses at 00 UTC 11 January, and results are shown from runs with 25- and 10-km grid distance. (a) SLP (hPa), (b) wind speed at 10 m (m s^{-1}), (c) temperature at 2 m (°C).

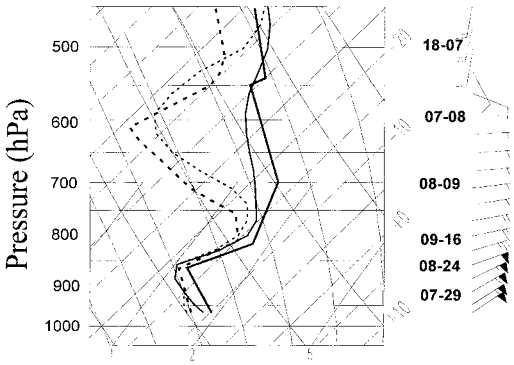

Fig. 4. Observed radiosonde ascent and simulated ascent for Bear Island 00 UTC 12 January 1993. The simulation was conducted with 25-km grid distance and was initialised by ECMWF analyses at 00 UTC 11 January. Solid lines show temperature and dashed lines dew-point temperature. The dashed lines represents the observations and the solid lines the simulation. An oblique *T*, ln *p* diagram is used. The numbers on the vertical axis denotes the temperature in Celsius degrees and the numbers on the horizontal axis denotes saturation mixing ratio. Observed wind direction (tens of degrees) and wind speed (m s^{-1}) are given in numbers on the right-hand side. Simulated wind is shown for selected model levels according to WMO's standard (wind from north down the paper).

inversion above a neutral boundary layer, is well simulated. However, some errors might be noted.

(1) The surface wind speed is 5 m s^{-1} weaker than the observed speed at the ship; still, a speed of 35 m s^{-1} is found at the top of the well-mixed boundary layer above the ship (see Table 1).

(2) The simulated surface temperature at Bear Island is systematically about 8 K too low in the 25 km simulation. Similar temperature errors are also found over the ice at Hopen. The reason for this discrepancy might partly be connected to uncertainties in the position of the ice edge.

In spite of the errors, we find the agreement between the simulations and the observations to be sufficiently close for further diagnosis of the episode.

The synoptic context of this event was deep northeast-bound extratropical cyclones over the ocean to the south of the arctic sea–ice. Fig. 5 shows the predicted surface map (SLP, temperature, wind speed at 925 hPa and surface fronts) at 12 UTC 11 January (+12 h) and at 06 UTC the next day (+30 h). The deep mature cyclone to the southwest decreases in intensity as it travels slowly northeasterly. A secondary trough develops over Northern Scandinavia at the triple point of the frontal system of the main low. This disturbance moves toward the northern tip of Norway. The frontal system occludes, and at 06 UTC 12 January the occlusion had passed the coast of Norway and become almost stationary in a zonal direction.

In the beginning of the simulation, an arctic air mass that originated over the sea–ice, is located over the sea (Fig. 5a). Strong heating from the ocean has formed a marked boundary layer with neutral or unstable stratification (Fig. 6a). This layer is capped by a zone of strongly stratified arctic air that forms an AF. At the surface, the AF is positioned between the coast of Norway and Bear Island. The arctic air mass extends far towards southwest. The AF remains over the area to the north of the occlusion throughout the simulation. The development is in reasonable agreement with Økland's analysis, with the exception of the frontal system in southeast, where the position of the fronts is uncertain because of the influence of surface inversions over the arctic continent.

A 400 km broad band of large temperature and pressure gradients are found at the surface north of the AF (Figs. 5a, b). In the area between Spitsbergen and Norway, the temperature range over the band is almost constant at 25 K between 12 UTC 11 January and 06 UTC the next day. However, as the occlusion approach from the south, the wind at the top of the boundary layer and the geostrophic wind at the surface increase from 20 and 30 m s^{-1} to 30 and 45 m s^{-1} respectively. At 12 UTC 11 January (+12 h), maximum wind of more than 30 m s^{-1} is found in a narrow band just north of the AF in southwest, on the northern side of the strong cyclone (Fig. 5a). At 06 UTC 12 January (+30 h) strong wind speeds (>30 m s^{-1}) is found in a much broader jet between the front and the southern tip of Spitsbergen (Fig. 5b and the cross-section in Fig. 6b). While the strong winds in the beginning of the simulation are connected to the mature cyclone further southwest, the strong wind in the Bear Island area is connected to the approach of the occlusion of the new cyclone development.

Since the thermal wind connected to the AF is

Table 1. *Sea level pressure (SLP) at three positions at 18°E, geostrophic wind speed between two positions in north and the two positions in south, maximum wind speed at the low-level jets at the ice edge and at the AF, and maximum fluxes of sensible heat from the ocean. The numbers are given every 3 h in simulations with 25- and 10-km grid length valid at 11 January 1993 12 UTC to 12 January 1993 12 UTC*

11 and 12 Jan. 1993. Time (UTC):	12	15	18	21	00	03	06	09	12
25 km									
SLP (hPa) 77°	994.1	994.4	994.8	995.2	996.3	996.0	996.5	995.5	996.7
SLP (hPa) 74° 30′	981.0	980.5	979.5	979.0	978.4	978.3	978.0	978.8	980.0
SLP (hPa) 72°	965.2	962.7	960.4	958.8	957.5	957.2	956.8	957.7	959.8
V_g (m s^{-1}) 77°–74° 30′	27.0	28.5	31.5	33.5	37.0	36.5	38.0	36.5	34.5
V_g (m s^{-1}) 74° 30′–72°	32.5	36.5	39.5	41.5	43.0	43.5	43.5	43.5	41.5
Max. wind speed N jet (m s^{-1})	25.5	26.0	28.0	29.0	30.5	33.0	33.0	34.5	34.0
Max. wind speed S jet (m s^{-1})	24.5	27.0	29.0	29.5	32.5	35.0	34.5	34.5	34.0
Max. sens. heat flux (W m^{-2})	1100	1150	1250	1250	1300	1300	1300	1260	1260
10 km									
SLP (hPa) 77°	994.2	993.6	994.2	995.0	996.1	995.4	995.5	995.8	995.8
SLP (hPa) 74° 30′	980.4	978.5	977.8	978.5	978.0	978.2	979.7	979.7	981.3
SLP (hPa) 72°	965.2	962.0	959.4	959.3	959.5	959.6	959.7	961.8	965.0
V_g (m s^{-1}) 77°–74° 30′	28.5	31.0	34.0	35.0	36.0	36.0	35.5	33.0	30.0
V_g (m s^{-1}) 74° 30′–72°	31.5	34.0	37.5	38.5	39.0	38.0	38.0	37.0	33.5
Max. wind spped N jet (m s^{-1})	28.0	29.0	30.0	31.5	32.0	33.0	34.0	33.5	32.5
Max. wind speed S jet (m s^{-1})	25.5	29.0	29.5	31.0	33.0	32.0	31.0	29.5	28.0
Max. sens. heat flux (W m^{-2})	1100	1150	1250	1300	1300	1250	1200	1150	1050

in the opposite direction of the surface wind, the strongest wind is found in a jet at the top of the boundary layer. The isobars are nearly straight, and at 925 hPa, which is close to the top of the boundary layer, the wind speed is generally 70% of the geostrophic wind speed. As will be shown later, the ageostrophic wind at the top of the surface layer is mainly along the pressure gradient, from the ice towards the AF at the surface, with a mean speed of 5–10 m s^{-1} at the top of the boundary layer. With this cross-frontal wind velocity v and cross-frontal horizontal scale $L_y = 400$ km, the Rossby number (Ro $= v/L_y f$) of the frontal circulation is of the order 0.1.

The strengthening of the wind north of the AF is related to the interaction of the low-level jet north of the AF with the easterly winds in advance of the approaching occlusion. This is clearly illustrated in cross-sections across the AF (section AA′ in Fig. 2) at 18 UTC 11 January (+18 h) and at 06 UTC 12 January (+30 h) shown in Fig. 6. The warm occlusion is found all through the troposphere with easterly winds at the surface and a westerly jet at the tropopause. At 06 UTC 12 January (+30 h) the two low-level jets have merged into one stronger jet, with maximum wind speed of 34.5 m s^{-1} (Table 1) at the top of the boundary layer at the southern part of the AF. Further details will be discussed in Section 3.3.

In addition to the AF described above, a shallower front is noted at the ice edge east of Bear Island. This front will be referred to as the ice edge front. It is characterized by strong temperature and pressure gradients in a narrow band along the ice edge. The flow along this front is highly ageostrophic, and there is a substantial cross-isobaric flow at the surface. The geostrophic wind equivalent of the maximum surface pressure gradient is 70 m s^{-1} (Fig. 7a). As seen in Fig. 7a, the actual simulated wind is only 30–50% of this.

3.2. *The off-ice flow*

Large values of sensible and latent heat are transferred from the sea to the air. The fluxes are large throughout the simulation and the increase in wind speed is accompanied by a slight increase in the heat fluxes (Table 1). The temporal change of the lower tropospheric flow is also rather modest and smooth for the period 12 UTC 11 January (+12 h) to 06 UTC 12 January (+30 h). This indicates a near balance of the lower

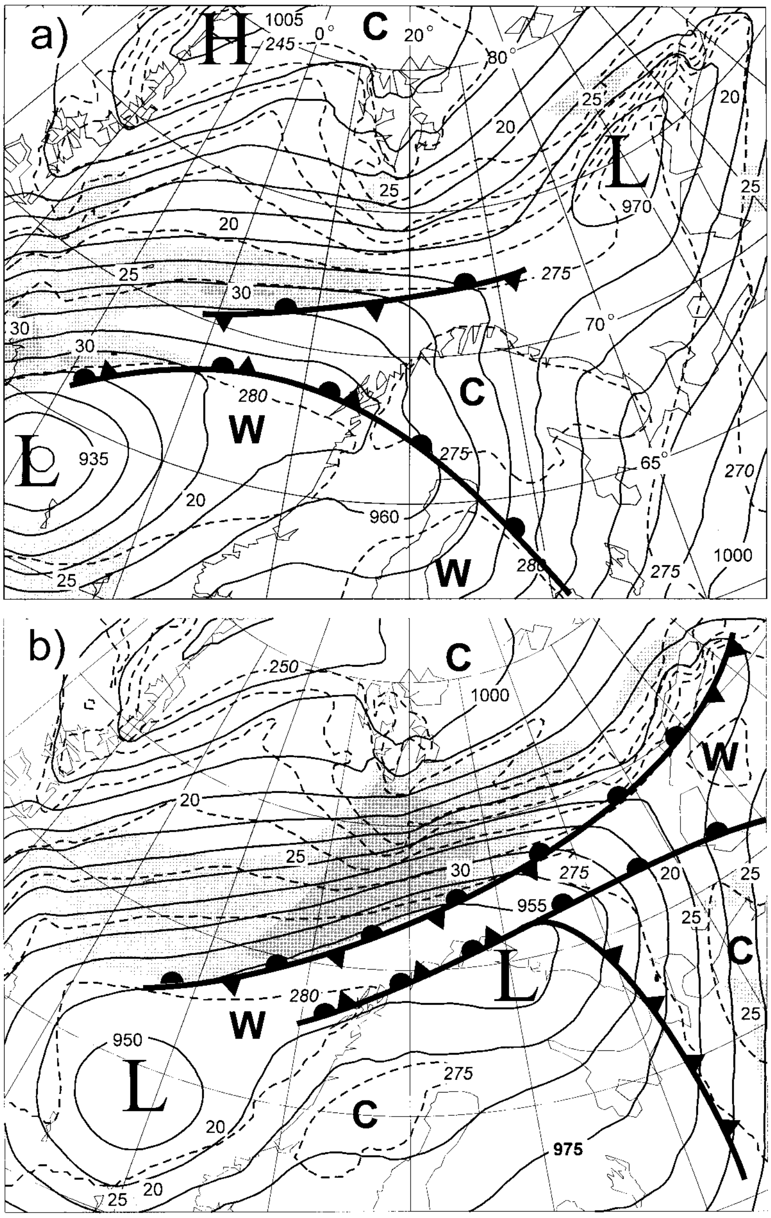

Fig. 5. Simulated surface maps valid at (a) 12 UTC 11 January 1993 and (b) 06 UTC 12 January 1993. The simulation was conducted with 25-km grid distance and was initialised by ECMWF analyses at 00 UTC 11 January. Two sets of isolines are shown: SLP (solid lines, contours every 5 hPa), potential temperature θ at 925 hPa (dashed lines, contours every 5 K). Wind speed at 925 hPa is indicated with grey shading (every 5 m s^{-1} from 20 m s^{-1} and above). Fronts are subjectively drawn, and the letters L, H, C, W indicate the position of lows and highs, minimum and maximum of cold and warm air.

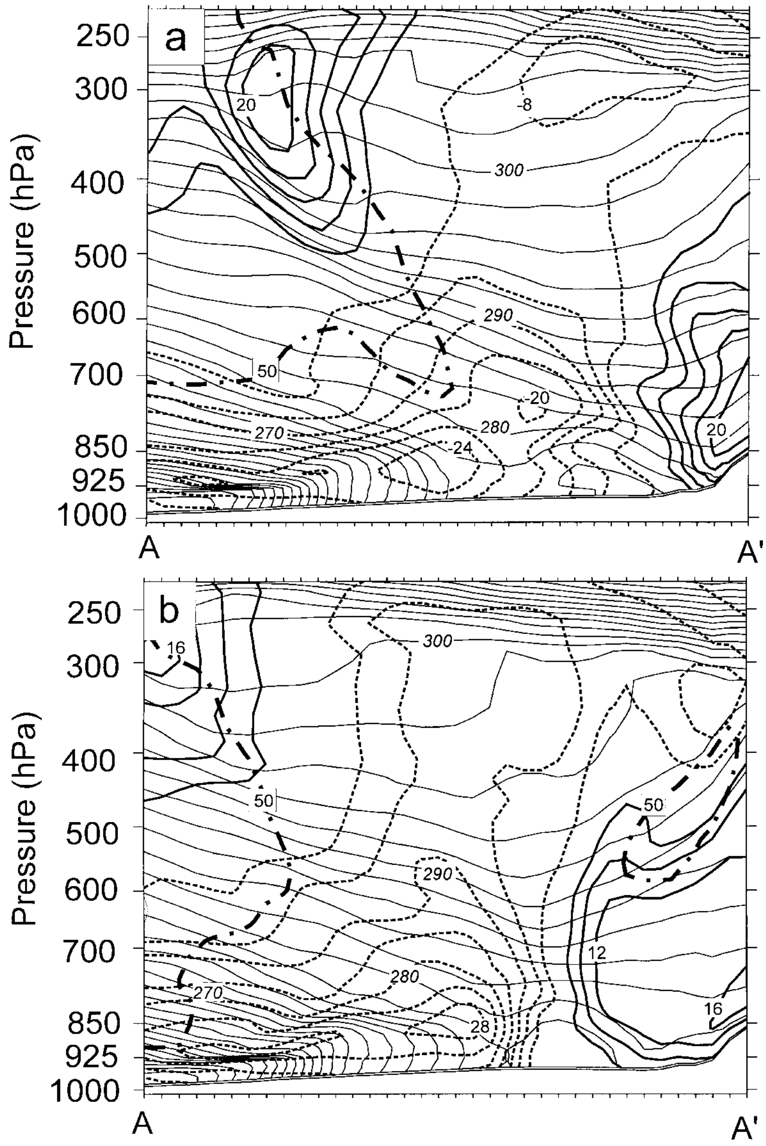

Fig. 6. Simulated parameters in cross-section AA′ (for position, see Fig. 2) valid at (a) 18 UTC 11 January and (b) 06 UTC 12 January. The simulation was conducted with 25-km grid distance and was initialised by ECMWF analyses at 00 UTC 11 January. The grid is indicated by the tick-marks on the horizontal axis. Three parameters are shown: potential temperature θ (solid lines, contours every 2 K), normal wind speed (contours every 4 m s^{-1}, heavy solid lines: positive values, into the paper, dashed lines: negative values, out of the paper, and broken dotted lines: zero normal wind), and relative humidity (one single contour showing 50% relative humidity).

tropospheric flow with the heating from the ocean. The sensible and latent heating at 00 UTC 12 January (+24 h) is shown in Fig. 7b. To the north of Bear Island, where the flow is perpendicular to the ice edge, sensible heat fluxes of more than 1200 W m^{-2} are simulated. The latent heat flux is smaller in magnitude and the maximum is shifted downwind from the ice edge. The balance

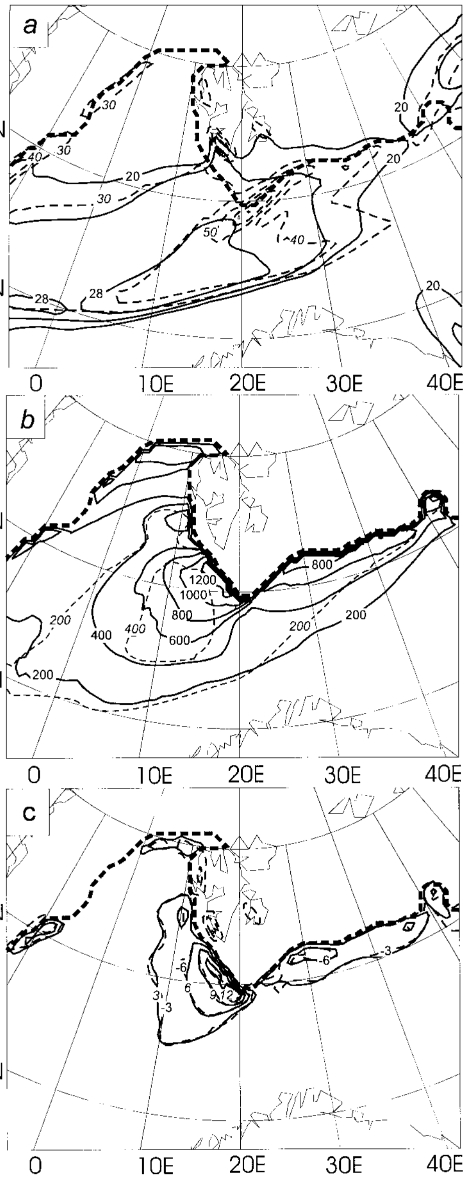

Fig. 7. Simulated parameters close to the surface at 00 UTC 12 January 1993. The simulation was conducted with 25-km grid distance and was initialised by ECMWF analyses at 00 UTC 11 January. Wind speed at the second lowest model layer (~ 100 m) (solid lines, contours every 4 m s^{-1} from 20 m s^{-1} and above) and geostrophic wind speed at 1000 hPa (dashed lines, contours every 10 m s^{-1} from 40 m s^{-1} and above). (a) Fluxes of sensible (solid lines) and latent heat (dashed lines). Contours every 200 W m^{-2}. (b) Diabatic sensible heating at the second lowest model layer (~ 100 m) (solid lines, contours every 3 K h^{-1}) and horizontal advection (dashed lines, contours with negative values every 3 K h^{-1}).

between the vertical convergence in the sensible heat flux and the temperature advection in the model can be seen in Fig. 7c. Since cold advection is grossly balanced by sensible heating from below, the temperature field is almost stationary. The balance between advection and heating within an arctic outbreak has been discussed by Shapiro and Fedor (1989). In the present study, however, the maximum heating is 20× higher than that found in their analyses. In the standard bulk aerodynamic formula the sensible heat flux is proportional to T_{sea}–T_{air} and the wind speed. The maximum T_{sea}–T_{air} simulated near the ice edge in this study is 30 K which is 6× the value of 5 K reported by Shapiro and Fedor. Furthermore, the wind modeled in the present study is 25 m s^{-1} versus 15 m s^{-1} in the case examined by Shapiro and Fedor.

We will more closely address the vertical structure of the AO extending from the ice edge towards southwest. Fig. 8 shows the flow in cross-section BB′ (for position, see Fig. 2). The convective boundary layer, capped by the inversion of arctic air, shows the characteristic downstream height increase from the ice in qualitative agreement with theoretical estimates given by Økland (1983), based on a constant SST, and measurements of an outbreak by Shapiro and Fedor (1989). The layer reaches its maximum height of 1500 m, 500 km downwind from the ice. With the nearly homogenous tangential wind speed in the convective layer, the maximum height is reached after 5–6 h transport of the cold air off the ice edge. We note the tendency for superadiabatic lapse rates to form through the lowest part of the layer. The heating rates, which in the figure also includes latent heating, have a maximum of 11 K h^{-1} close to the ice edge and decreases to about 1 K h^{-1} at the position of maximum height. The latent heating at the top of the layer is less than 1 K h^{-1}.

The relative humidity (RH) has an interesting distribution. The air close to the ice edge is saturated through the boundary layer for a distance of 100 km. In this way the simulation gave sea smoke, a phenomenon which has been studied extensively (Rodhe, 1962; Saunders, 1964; Økland, 1983). We have investigated satellite images for the area, but sea smoke seems to be difficult to identify from such data. With the large air to sea temperature difference close to the ice edge, the necessary conditions for sea smoke to develop are

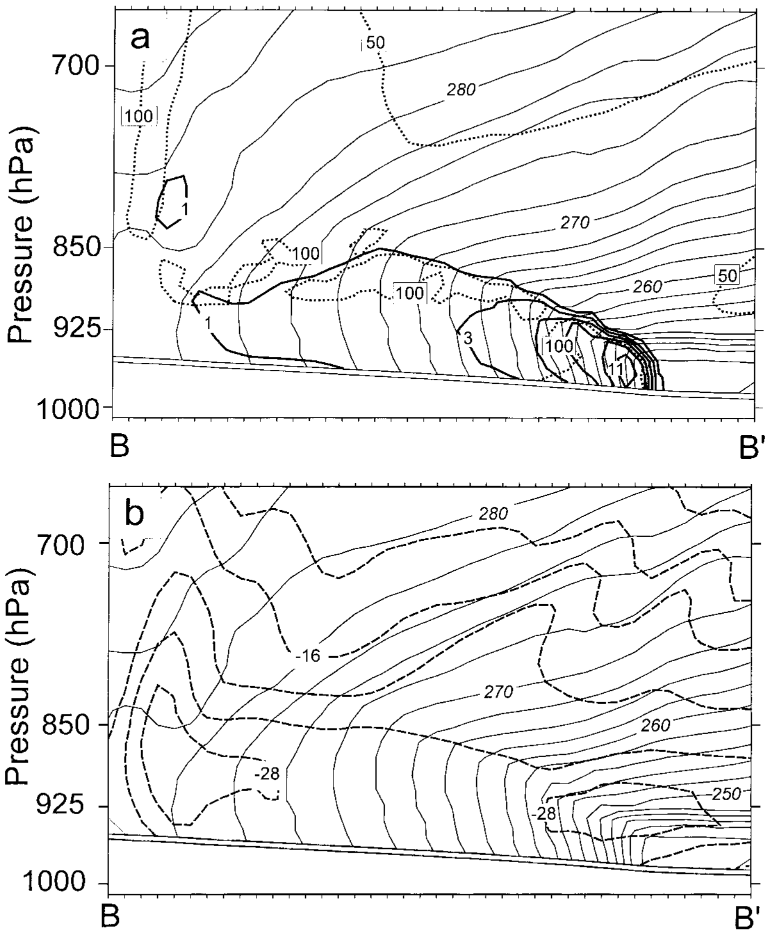

Fig. 8. Simulated parameters in cross-section BB′ (for position, see Fig. 2) valid at 00 UTC 12 January 1993. The simulation was conducted with 25-km grid distance and was initialised by ECMWF analyses at 00 UTC 11 January. There is 25 km between the tick-marks on the horizontal axis. (a) Equivalent potential temperature θ_e (solid lines, contours every 2 K), sensible and released latent heating (heavy solid lines, contours at 1, 3, 5, 7, 9 and 11 K h^{-1}) and relative humidity (contours at 50 and 100%). (b) Potential temperature θ (solid lines, contours every 2 K) and tangential wind component (dashed lines, contours every 4 m s^{-1}, negative to the left).

satisfied. Further downstream, the air is saturated only at the top of the mixed layer where some precipitation is produced. The humidity distribution is in agreement with Økland, who noted that sea smoke frequently occurs near the ice edge in AOs when the boundary layer is shallow and the air to sea temperature differences are large. Further downstream, the sea smoke disappears and the humidity is sufficient for cumulus and stratocumulus to form in the upper part of the boundary layer.

3.3. The arctic front and the occlusion

The strong surface wind in the boundary layer north of the AF occurred when the occlusion approached the AF from south. As can be seen from Table 1, the most rapid increase in the low-level jet at the AF occurred between 21 UTC 11 January (+21 h) and 03 UTC 12 January (+27 h) in the model, i.e., 3 h later than the observed wind increase at the ship. The modeled change in the maximum wind is 6 m s^{-1}, while the increase at the ship is 9 m s^{-1}. We will study the circulation of the fronts with emphasis on this period with the greatest change in the wind speed. Fig. 9 shows fields of the flow in a cross-section just east of Bear Island (section CC′ in Fig. 2), parallel to the pressure gradients at the surface at 21 UTC 11 January (+21 h) and 03 UTC 12 January (+27 h).

The approach of the occlusion towards the southern edge of the AF has already been shown in Fig. 6. The occlusion is hard to identify at the surface because of topographical effects and cold surface air over the continent. At 18 UTC 11 January the warm occlusion aloft is clear through the troposphere with an easterly jet in the lower troposphere and a westerly jet at the tropopause (Fig. 6a). Maximum normal wind component in the easterly jet is 20 m s^{-1} at 800 hPa. Furthermore, ahead of the front a dry intrusion is seen from a tropopause folding at the jet and down to 850 hPa. The distance between the core of the jet in advance of the warm front and the southern edge of the AF is approximately 50 km. The height of the convective layer is almost constant and rather homogenous in a broad jet, but with an increase towards the southern edge. Between the arctic air in the frontal zone of the AF and the warm air south of the warm front, we find air masses with much smaller horizontal temperature gradients. This is clearly shown in the equivalent potential temperature (θ_e) in Figs.

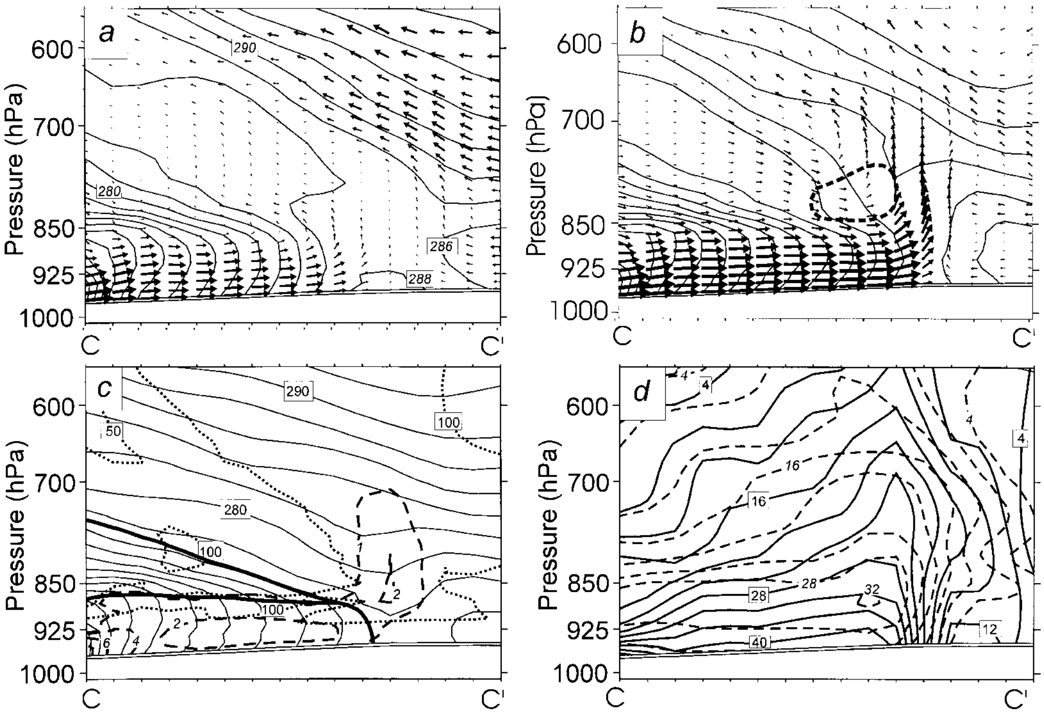

Fig. 9. Simulated parameters in cross-section CC′ (for position, see Fig. 2). The simulation was conducted with 25-km grid distance and was initialised by ECMWF analyses at 00 UTC 11 January. The grid is indicated by the tick-marks on the horizontal axis. (a) 21 h simulation of equivalent potential temperature θ_e (solid lines, contours every 2 K) and the vertical circulation illustrated with arrows, which are trajectories for half an hour. (b) 27 h simulation of the same parameters as in (a). In addition, an area of conditional symmetric instability (CSI) is marked with a heavy dotted line. (c) 27 h simulation of potential temperature θ (solid lines, contours every 2 K), sensible and released latent heating (broken heavy lines with contours for 1, 2, 4, 6 and 8 K h^{-1}) and relative humidity (dotted lines, contours for 50 and 100%). The extension of the frontal zone of the arctic front is shown with heavy solid lines. The southern edge of the front is marked with a single line. (d) 27 h simulation of the normal component of the wind (dashed lines) and normal component of geostrophic wind (solid lines). Contours are given for every 4 m s^{-1}, and the direction is everywhere out of the paper for both components.

9a, b. In the same figures the temperature distribution shows an interesting structure at the southern part of the AF. While the northern part consists of a zone of stably stratified air above the boundary layer, the southern part of the front does not contain any original cold arctic air at all. At 21 UTC 11 January the equivalent potential temperatures have typical values of the air mass between the two fronts. The southern part of the convective boundary layer has evidently been heated by sensible heat and release of latent heat. In Fig. 9c we have indicated the structure by drawing two lines, which show the stable AF zone of arctic air at the top of the boundary layer, and a single line as a continuation southwards at the top of the convective boundary layer where the air has been heated. We will refer to this sloping line as the edge of the front.

At 21 UTC 11 January, the 2 fronts have still their separate vertical circulations (Fig. 9a). At the AF there is convergence at the surface and the warm air is ascending. Condensation and release of latent heat takes place. At the occlusion there is another area with maximum ascending air at 800 hPa on the southern flank of the easterly jet. Also here condensation occurs and the air is heated. The lifting takes place some distance ahead of the occlusion at the surface, which is found at the Norwegian coast. The reason for this is probably connected to topographical effects in the lee of the mountains. The 2 areas with condensation and release of latent heat give relatively high temperatures between the fronts and low static stability. In this way interaction of the two jets can easily take place.

As the occlusion moves slowly northwards towards the stationary AF, the two easterly jets merge into one stronger jet at the top of the edge of the AF, with one area of ascending air between the two fronts (Fig. 9b). The vertical circulation is strengthened and the release of latent heat becomes stronger (Fig. 9c).

The frontal circulation shows a normal wind component approximately in geostrophic balance above the boundary layer (Fig. 9d), but the tangential wind component, which is dominated by the flow out from the ice in the boundary layer, is far from geostrophic balance. In this respect the circulation seems to follow semi-geostrophic frontal theory. The diabatic heating seems to indicate that release of latent heat is the main forcing for the vertical circulation (Fig. 9c). The gradients in the sensible heat fluxes at the surface are relatively small and the fluxes are balanced by cold advection. There is no return flow at the top of the zone of the AF. However, the vertical velocities and the return flow is connected to the occlusion.

At 03 UTC 12 January (+27 h), the warm side cross-frontal flow has a strange circulation above the AF, just north of the maximum updrafts (Fig. 9b). This circulation seems to be caused by symmetric instability, since an area of conditional symmetric instability (CSI) is present (CSI is discussed in standard textbooks, e.g., Holton, 1992). The identification of the area of CSI has been found by comparing the tilts with height of the isolines of absolute momentum $M = v + fy$ (v and y are the velocity normal to the front and the coordinate in the same direction, measured positive southwards in the figures) and θ_e. Small areas of CSI are present above the AF nearly all the time, but the area is largest and a vertical circulation is clearest seen at 03 UTC 12 January.

3.4. The front at the ice edge

The small scale of the circulation at the ice edge front is better resolved in the 10 km simulation and will be discussed on the basis of this run. The long straight ice edge to the east of Bear Island along which the flow is aligned at 00 UTC 12 January, is suitable for 2-dimensional studies. Fig. 10 shows the circulation in cross-section DD′ perpendicular to the edge (for position, see Fig. 2).

The horizontal scale across the front is of the order 100 km, the front is shallow and the vertical circulation is confined below 850 hPa. A large temperature difference of 13 K is found over 25 km at the surface just at the sea side of the edge (Fig. 10b). We have marked the front as the tilting zone with very stable air from these surface gradients towards a very stable layer over the ice, between a shallow boundary layer and 900 hPa. At the warm side of the front, there is an abrupt increase of the height of the mixed layer to about 1300 m. This height is nearly constant towards the southern edge of the cold air connected to the AF.

The pressure gradient and the geostrophic wind are naturally increased over the strong temperature gradients at the surface, and maximum values of 50 m s^{-1} are found in the cross-section.

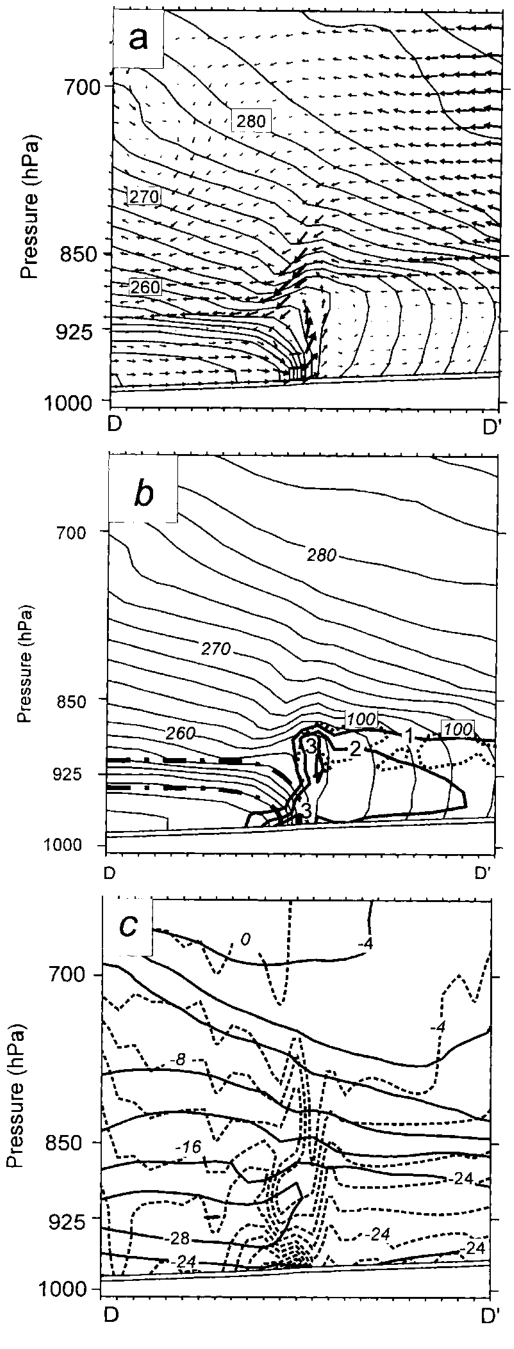

Fig. 10. Simulated parameters in cross-section DD′ (for position, see Fig. 2) valid at 00 UTC 12 January 1993. The simulation was conducted with 10-km grid distance and was initialised by ECMWF analyses at 00 UTC 11 January. The grid is indicated by the tick-marks on the horizontal axis. (a) Equivalent potential temperature θ_e (solid lines, contours every 2 K) and the vertical circulation illustrated with arrows, which are trajectories for half an hour. (b) Potential temperature θ (solid lines, contours every 2 K), sensible and released latent heating (heavy solid lines, contours at 1, 2 and 3 K h^{-1}) and 100% of relative humidity (heavy dotted lines). (c) Normal wind components (negative: out of the paper). Solid lines: wind, dashed lines: geostrophic wind. Contours are drawn for every 4 m s^{-1}.

The strongest normal wind component at the surface is found just south of the front where the vertical mixing is large (Fig. 10c). Because of some influence of gravity waves, the geostrophic wind aloft shows a noisy structure. However, it is clear that the normal wind component is generally further from geostrophic balance in the lowest layers than at the AF. This is connected to the small scale of the circulation (high Rossby number) and the limited extension of the front along the ice edge. The strongest normal wind is found over the ice within the frontal zone where the wind is super-geostrophic.

There is a marked vertical circulation connected to the ice edge front (Fig. 10a). The circulation is connected to the diabatic heating, mainly release of latent heat, above the sloping front (Fig. 10b). The vertical circulation is found around the area with the strongest gradients in the diabatic heating. The upper branch of the flow extends northwards in the relatively warm air above the frontal zone. At the surface over the ice, the cold flow is southwards. Strong sensible heating is found at the surface; however, this heat source is again grossly balanced by advection.

Generally, the wind speed at the ice edge front increases steadily from 12 UTC 11 January (+12 h) to 06 UTC 12 January (+30 h) (Table 1), maximum normal component of the geostrophic wind increases with 10 m s^{-1} and the maximum normal wind component at 925 hPa with 7 m s^{-1}. Since the wind is generally increased below 700 hPa, and since the frontal circulation does not change much after 12 UTC 11 January (+12 h), the increase seems to be related to a general wind increase as the warm occlusion is approaching. However, some of the increase is also due to a strengthening of the front by the frontal circulation.

4. Concluding remarks

Strong wind in the Arctic is normally connected to polar lows or strong topographic influence in flows with very strong stratification in lower layers. Unexpectedly, a Norwegian coast guard ship experienced hurricane force northeasterly winds in an arctic air mass south of Bear Island in the morning of 12 January 1993. Neither polar lows nor topographical effects were present. In this paper, the development of the storm was studied by means of a numerical model. It was shown that the strong wind was associated with a boundary layer jet north of a quasi-stationary AF over the sea between Bear Island and north Norway. The wind speed increased as an occlusion approached from the south. Easterly wind was found in advance of the occlusion and the strongest wind event was a result of an interaction of the wind at the occlusion with the jet at the arctic front. Arctic fronts in association with synoptic activity are frequent in this area in winter. There is therefore reasons to believe that meteorological conditions similar to those documented in this paper, often produce strong winds in the Arctic. It is not unlikely that some of the accidents mentioned in the introduction are caused by AFs. Since the east and northeasterly winds have a large component parallel to the ice edge, and since the drift of the sea–ice is to the right of the wind direction, ships may get trapped and crushed in the pack ice.

A strong, nearly straight surface flow from the arctic sea ice and out over the warm sea was found for a period of more than 24 h. The sea–ice had a characteristic shape for the season, with the ice edge extending eastwards and northwards towards Spitsbergen from a corner just North of Bear Island. The surface wind increased as the occlusion approached, however, the temperature conditions with strong gradients from the cold air over the ice towards the AF over the sea, did not change much. The sensible heating from the ocean was very strong with fluxes reaching more than 1200 W m^{-2}. The heating formed a typical convective boundary layer, with increasing heights from the ice edge in qualitative agreement with theory and field measurements. Similar modeled fluxes have been reported by Mailhot et al. (1996). The task of getting measurements under such extreme conditions is an almost impossible one. The strongest flux based on observations known to the authors is 800 W m^{-2} measured in a polar low by Shapiro et al. (1987). In our simulations, the heating rates were very high, more than 10 K h^{-1} was found close to the ice edge where the temperature difference between sea and air was 30 K. It was shown that this heating was almost balanced by cold air advection.

The strong surface wind was found in a broad band (400 km) north of the surface arctic front. The broad northward extension of the wind was due to a second, even more shallow front at the ice edge. There were consequently two quasi-stationary arctic fronts oriented in a almost zonal direction. The model simulated distinct secondary circulations associated with these fronts. These circulations were not solely forced by geostrophic deformations. The main front transversal circulation was forced by latent heat release on the warm side.

The circulation at the ice edge front was subject to forcing due to differential surface sensible heating. Økland (1998) investigated the transverse frontal circulation in an ice edge front and solved the Sawyer–Eliassen equation with prescribed sensible heating rates. The conclusion of that interesting paper is that a sensible heat flux of 500 W m^{-2} might result in an increase in the along front wind speed of 10 m s^{-1}. In Fig. 7a we showed pressure gradients across the ice edge that would require a wind speed along the ice edge of 70 m s^{-1} in order to balance the flow geostrophically. However, the limited extension of this sensible heat forcing along the ice edge did not provide a sufficient time scale for geostrophic adjustment, and the flow configuration showed a large cross-isobaric component. The basic assumptions of semi-geostrophic theory is consequently violated. The magnitude of the temperature and pressure gradients across the ice edge in our simulations is probably somewhat overestimated due to the lack of representation of the marginal ice zone (MIZ) in the model. This might explain the cold biases at Bear Island and Hopen. Inclusion of a MIZ would presumably spread the sensible heating over a larger area and thereby reduce the sensible heating rates.

5. Acknowledgements

The authors wish to thank Kari Wilhelmsen for information concerning ship disasters in the Arctic.

Discussions with Professor Elmer Raustein are highly appreciated. The super-computing time has been made available by The Norwegian Research Council.

REFERENCES

Bluestein, H. B. 1992. *Synoptic-dynamic meteorology in midlatitudes*. Oxford University Press.

Busch, N., Ebel, U., Kraus, H. and Schaller, E. 1982. The structure of the subpolar inversion capped ABL. *Arch. Meteor. Geophys. Bioklimatol.* **331**, 1–18.

Carlson, T. N. 1991. *Mid-latitude weather systems*. Harper Collins Academic, 507 pp.

Curry, J. A. 1983. On the formation of continental polar air. *J. Atmos. Sci.* **40**, 2279–2292.

Curry, J. A., Rossow, W. B., Randell, D. and Schramm, J. M. 1996. Overview of Arctic cloud and radiation characteristics. *J. Climate* **9**, 1731–1764.

Davies, H. 1976. A lateral boundary formulation for multilevel prediction models. *Quart. J. Roy. Met. Soc.* **102**, 405–418.

Eliassen, A. 1952. Slow thermally and frictionally controlled meridional circulations in a circular vortex. *Astrophysica Norvegica* **5**, 19–60.

Eliassen, A. 1959. On the formation of fronts in the atmosphere. *The Rossby memorial volume*. Rockefeller Institute and Oxford University. N.Y., 247–260.

Eliassen, A. 1962. On the vertical circulation in frontal zones. *Geophysica Norvegica* **24**, 147–160.

Eliassen, A. 1990. Transverse circulation in frontal zones. In: *Extratropical cyclones. The Erik Palmén Memorial Volume*. Amer. Meteorol. Soc., Boston, 155–165.

Furevik, T. 1998. *On the Atlantic water flow in the Nordic Seas: bifurcation and variability*. Dr. Thesis, Geophysical Institute, University of Bergen, Norway.

Godske, C. L., Bergeron, T., Bjerknes, J. and Bundgaard, R. C. 1957. *Dynamic meteorology and weather forecasting*. Amer. Meteorol. Soc., Boston, 800 pp.

Grønås, S. and Hellevik, O. E. 1982. *A limited area prediction model at the Norwegian Meteorological Institute*. Tech. Rep. no. 61. The Norwegian Meteorological Institute, 75 pp.

Haltiner, G. and Williams, R. 1980. *Numerical prediction and dynamic meteorology*. John Wiley and Sons, N.Y.

Holton, J. R. 1992. *An introduction to dynamic meteorology*, 3rd edition, Academic Press Inc., 511 pp.

Hoskins, B. J. and Bretherton, F. P. 1972. Atmospheric frontogenesis: mathematical formulation and solution. *J. Atmos. Sci.* **29**, 11–37.

Louis, J. 1979. A parametric model of vertical eddy fluxes in the atmosphere. *Boundary-Layer Meteorol.* **17**, 187–202.

Mailhot, J., Hanley, D., Bilodeau, B. and Hertzman, O. 1996. A numerical case study of a polar low in the Labrador Sea. *Tellus* **48A**, 383–402.

Maykut, G. A. and Church, P. E. 1973. Radiation climate of Barrow, Alaska 1962–1966. *J. Appl. Meteor.* **12**, 620–628.

Nordeng. T. E. 1986. *Parameterization of physical processes in a 3-dimensional numerical weather model*. Tech. Rep. no. 65. The Norwegian Meteorological Institute, Oslo, Norway.

Økland, H. 1983. Modelling the height, temperature and relative humidity of a well-mixed planetary boundary layer over a water surface. *Boundary-Layer Meteorol.* **25**, 121–141.

Økland, H. 1998. Modification of frontal circulations by surface heat flux. *Tellus* **50A**, 211–218.

Palmén, E. and Newton, C. 1969. *Atmospheric circulation systems*. Academic Press.

Rohde, B. 1962. The effect of turbulence on fog formation. *Tellus* **14**, 49–86.

Saunders, P. M. 1964. Sea smoke and steam fog. *Quart. J. Roy. Met. Soc.* **90**, 155–165.

Sawyer, J. S. 1956. The vertical circulation at meteorological fronts and its relation to frontogenesis. *Proc. Roy. Soc. London* **A234**, 346–362.

Serreze, M. C., Kahl, J. D. and Schnell, R. C. 1992. Low-level temperature inversions of the Eurasian Arctic and comparisons with Soviet ice island data. *J. Climate* **8**, 599–613.

Serreze, M. C., Box, J. E., Barry, R. J. and Walsh, J. E. 1993. Characteristics of Arctic synoptic activity. *Meteorol. Atm. Phys.* **51**, 147–164.

Shapiro, M. A. and Fedor, L. 1989. A case study of an ice edge boundary layer front and polar low development over the Norwegian and Barents Sea. In: *Polar and Arctic lows*. A. Deepack Publishing, 257–277.

Shapiro, M. A. and Grell, E. D. 1994. In search of synoptic/dynamic conceptualizations of the life cycles of fronts, jet streams, and the tropopause. In: *The life cycles of extratropical cyclones*. Geophysical Institute, University of Bergen, 163–192.

Shapiro, M. A., Hampel, T. and Fedor, L. S. 1987. Research aircraft measurements of a polar low over the Norwegian Sea. *Tellus* **39A**, 272–306.

Shapiro, M. A., Hampel, T. and Fedor, L. 1989. Research aircraft observations of an Arctic front over the Barents Sea. In: *Polar and Arctic lows*. A. A. Deepak, Publishing Hampton, Va, 279–289.

Skeie, P. and Grønås, S. 1999. Strongly stratified flows across Spitsbergen. *Tellus*, submitted.

Sverdrup, H. U. 1933. *The Norwegian North Polar Expedition with the "Maud", 1918–1925. Scientific Results*, vol. 1a. Geofysisk Institutt, 331 pp.

Thorpe, A. J. and Emanuel, K. A. 1985. Frontogenesis in the presence of small stability to slantwise convection. *J. Atmos. Sci.* **42**, 1809–1824.

Vowinkel, E. and Orvig, S 1970. The climate of the North Polar Basin. *Climates of the polar regions*, vol. 14. *World Survey of Climatology* (Ed. Orvig, S). Elsevier, 129–152.

Wexler, H. 1936. Cooling in the lower atmosphere and the structure of polar continental air. *Mon. Wea. Rev.* **64**, 122–136.